View Article Online
DOI: 10.1039/C8TC03170C

Journal Name

ARTICLE

Plasmonic Properties of Ag@$Ag_2Mo_2O_7$ Hybrid Nanostructure Easily Designed by Solid-state Photodeposition from Very Thin $Ag_2Mo_2O_7$ Nanowires

Received 00th January 20xx,
Accepted 00th January 20xx

DOI: 10.1039/x0xx00000x

www.rsc.org/

Hélène Serier-Brault,[a,*‡] Luc Lajaunie,[a,b,*‡] Bernard Humbert,[a] Raul Arenal,[b,c] and Rémi Dessapt [a,*]

A new Ag@*m*-$Ag_2Mo_2O_7$ plasmonic hybrid nanostructure was designed by an easy two-step synthesis method. Firstly, very thin photosensitive monoclinic *m*-$Ag_2Mo_2O_7$ nanowires (NWs) were synthesized under ambient pressure and at low temperature by using $Ag_2Mo_3O_{10}{\cdot}2H_2O$ NWs as a pre-nanostucturated starting material. This innovative soft chemistry route offers some precise control over the purity, the structure and the nanostructuration of the *m*-$Ag_2Mo_2O_7$ NWs that exhibit a very thin diameter around 100 nm, and a superior specific surface area compared to previously reported synthesis methods. Secondly, the plasmonic hybrid nanostructure Ag@*m*-$Ag_2Mo_2O_7$ was easily *in situ* obtained, *via* an all solid-state photodeposition method, by irradiating the *m*-$Ag_2Mo_2O_7$ NWs under low energy and low-power UV-light. The composition, morphology and plasmonic properties of the nanocomposite were investigated by a combination of energy X-ray dispersive microscopy, high-resolution scanning transmission electron microscopy, X-ray photoelectron spectroscopy and Auger spectroscopy, Near-infrared, Raman and UV-vis spectroscopies as well as spatially-resolved electron energy-loss spectroscopy. A plausible mechanism explaining the formation of the nano-heterostructure under irradiation was also discussed. The Ag@*m*-$Ag_2Mo_2O_7$ nanostructure manifests interesting plasmonic properties and particulary a high Surface-Enhanced Raman Scattering (SERS) sensitivity probed by 2,2'-bipyridine.

INTRODUCTION

Plasmonic hybrid nanostructures assembling nanoparticles (NPs) of noble metal (i.e. Ag, Au, Pt) and metal-oxide nanowires (NWs) are the focus of current research efforts in nanotechnology[1–3] since they combine the localized surface plasmon resonance (LSPR) of the metals NPs with the specific photochemical properties of semiconducting NWs. On the one hand, due to their high surface-to-volume ratio and low radial dimension, metal-oxide NWs favor fast diffusion rates of photo-excited carriers at the surface with respect to electron-to-hole recombination processes, and anisotropic carrier transport along the growth direction.[4,5] On the other hand, metal NPs improve charge separation at the metal-semiconductor interface and allow injection of hot electrons into the semiconductor.[6] The synergetic coupling of these optical features has been recently exploited in many domains involving light trapping and electromagnetic field enhancement such as photocatalysis for pollutant and bacterial destruction, enzyme surrogates,[7–10] photoelectrochemical water splitting,[1,11] solar energy conversion,[12,13] biosensing,[14] and Surface Enhanced Raman Scattering (SERS).[15–17] All these applications require metal-oxide NWs with high specific surface areas to optimize absorption of light, to improve interactions with noble metal NPs, and to increase the adsorption of reactive species.

The main synthesis methods to design such plasmonic hybrid nanostructures consist in decorating metal-oxide semiconductors with metal NPs prepared separately[11–13] or *in situ* photodeposited by reduction under high-power UV irradiation (100-500 W) of Ag^+-containing solutions.[18,19] For example, the facile solution-based photoreduction process was successfully employed to design new hematite/Ag and ZnO/Ag hierarchical nanostructures which were applied as a photoanode in photo-electrochemical cells for water splitting applications.[20-22] A novel approach using a non-aqueous sol-gel process based on the low-temperature synthesis route has also been recently reported.[23] However these methods require a solid-liquid interface that often hinders a precise control of the NPs size distribution and provide an inhomogeneous coverage onto the semiconductor surface. Recently, we demonstrated the possibility of easily designing Ag@metal-oxide semiconductor hybrid nanostructures from

[a] *Institut des Matériaux Jean Rouxel, Université de Nantes, CNRS, 2 rue de la Houssinière, BP32229, 44322 Nantes Cedex 3, France. *Email : helene.brault@cnrs-imn.fr, remi.dessapt@cnrs-imn.fr*
[b] *Laboratorio de Microscopías Avanzadas, Instituto de Nanociencia de Aragón, Universidad de Zaragoza, 50018 Zaragoza, Spain. E-mail: lajaunie@unizar.es*
[c] *ARAID Foundation, 50018 Zaragoza, Spain.*
‡ H. Serier-Brault and L. Lajaunie contributed equally.

Electronic Supplementary Information (ESI) available: Rietveld refinement of the powder X-ray diffraction (PXRD) data and TGA/DSC curves of *m*-$Ag_2Mo_2O_7$ NWs ; UV-vis, Ag 3d, Mo 3d XPS and Auger electron spectra of *m*-$Ag_2Mo_2O_7$ NWs and Ag@*m*-$Ag_2Mo_2O_7$ NWs ; additional PXRD patterns ; SEM micrograph of *m*-$Ag_2Mo_2O_7$ microrods ; HR-TEM micrographs, SR-EELS and Near Infrared spectra of Ag@*m*-$Ag_2Mo_2O_7$ NWs. See DOI: 10.1039/x0xx00000x

photosensitive silver molybdates via an alternative all solid-state photodeposition method.[24] Indeed, the Ag@$Ag_2Mo_3O_{10}$·$2H_2O$ nanostructure was obtained by exposing ultra-thin $Ag_2Mo_3O_{10}$·$2H_2O$ NWs under a low-power UV irradiation (6W). The proposed formation mechanism involves the photo-reduction of the polymeric 1D-$[Mo_3O_{10}]^{2-}$ unit coupled with the formation of highly reactive Ag^{2+} intermediary species, which are then easily reduced to Ag^0 NPs at the surface of the NWs. The Ag@$Ag_2Mo_3O_{10}$·$2H_2O$ nanocomposite is an efficient visible-light-driven plasmonic photocatalyst for degradation of Rhodamine B dye in aqueous solution. However, the 1D-$[Mo_3O_{10}]^{2-}$ block is difficult to photoreduce,[25] and the formation of the plasmonic hybrid nanostructure needs high-energy UV-light (254 nm) and relatively long UV-irradiation time (4h). Consequently, we aim at transposing our approach to more easily photoreducible silver molybdates. For this purpose, $Ag_2Mo_2O_7$ is a very promising candidate, because it also contains polymeric 1D-$[Mo_2O_7]^{2-}$ units (Figure 1a) i.e., a suitable topology to reach nanowire-like morphologies. In addition, $Ag_2Mo_2O_7$ exhibits a bandgap of c.a 2.7-2.9 eV[26,27] what would allow generating photo-excited charge carriers with low-energy UV-light. However, controlling both the purity and the nanostructuration of $Ag_2Mo_2O_7$ as very thin NWs with high specific surface areas still remains very challenging.

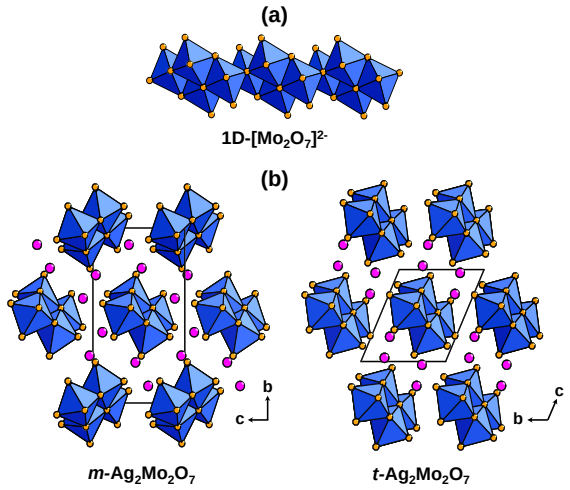

Figure 1. (a) Polyhedral representation of the polymeric 1D-$[Mo_2O_7]^{2-}$ block. (b) Crystal structures of monoclinic *m*-$Ag_2Mo_2O_7$ (left) and triclinic *t*-$Ag_2Mo_2O_7$ (right) viewed perpendicular to the *bc* plane, the 1D-$[Mo_2O_7]^{2-}$ chains running along the *a*-axis (blue octahedra = MoO_6; magenta spheres: silver; orange spheres: oxygen).

Traditional hydrothermal and more recent microwave methods were commonly used to design nano- and microstructurated $Ag_2Mo_2O_7$ with various morphologies such as nanoparticles,[8] nanowires,[28–30] nanoflowers,[31] broom-like microstructures,[31] or micro-rods.[31–33] However, it was often obtained impure with other silver molybdates,[16,34–36] and the composition of the mixtures is extremely pH-dependent.[31,34,37] Beside $Ag_2Mo_2O_7$ exhibits both monoclinic (*m*-$Ag_2Mo_2O_7$)[38] and triclinic (*t*-$Ag_2Mo_2O_7$)[39] polymorphs (Figure 1b) that can co-precipitate,[31] and the synthesis parameters governing their relative stability remain still unclear. Recently, pure *t*-$Ag_2Mo_2O_7$[28,29] and *m*-$Ag_2Mo_2O_7$[40] NWs with an average diameter of 200-500 nm were obtained from different synthesis routes, but the hydrothermal treatments that favor the crystal growth dramatically impact the nanostructuration, and the obtained materials exhibited a very low specific surface area of c.a 2 m^2/g.

We report herein the successful synthesis of a new Ag@*m*-$Ag_2Mo_2O_7$ plasmonic hybrid nanostructure *via* a facile two-step procedure. In a first step, very thin *m*-$Ag_2Mo_2O_7$ NWs with a high specific surface area were designed under ambient pressure and at low temperature from ultra-thin $Ag_2Mo_3O_{10}$·$2H_2O$ NWs. Both the purity and the nanostructuration of the targeted material are extremely temperature-, pressure- and time-dependent. In a second step, the Ag@*m*-$Ag_2Mo_2O_7$ hybrid nanostructure was designed by exposing the photosensitive *m*-$Ag_2Mo_2O_7$ NWs under a low-power UV irradiation. Strikingly, the solid-state photodeposition of Ag NPs at the surface of the *m*-$Ag_2Mo_2O_7$ NWs requires much lower energy UV-light (365 nm) and a much shorter irradiation time (40 min) than for generating the Ag@$Ag_2Mo_3O_{10}$·$2H_2O$ nanocomposite. The Ag@*m*-$Ag_2Mo_2O_7$ hybrid nanostructure was characterized by scanning electron microscopy (SEM), energy-dispersive X-ray spectroscopy (EDS), high-resolution scanning transmission electron microscopy (HR-STEM), Auger spectroscopy and X-ray photoelectron spectroscopy (XPS), that well evidence the presence of aggregates of metallic silver nanoparticles at the surface of the nanocomposite. The formation mechanism of the nanostructure is also discussed. Finally, the plasmonic activity of the nanocomposite has been highlighted by a combination of UV-vis, spatially-resolved electron energy-loss spectroscopy (SR-EELS) and SERS by using the molecular probe 2,2'-bipyridine.

RESULTS AND DISCUSSION

Synthesis and characterization of very thin *m*-$Ag_2Mo_2O_7$ NWs. All chemicals and reagents were purchased from major chemical suppliers and used as received except $Ag_2Mo_3O_{10}$·$2H_2O$ NWs which were prepared according to the reported procedure.[24] Very thin *m*-$Ag_2Mo_2O_7$ NWs were synthesized with a high yield (95 % in Mo), under ambient pressure and mild conditions (70°C/3h), from an aqueous slurry of $Ag_2Mo_3O_{10}$·$2H_2O$ NWs, one fold of Ag^+ ions and one fold of NaOH. Indeed, considering that the $[Mo_3O_{10}]^{2-}$ and $[Mo_2O_7]^{2-}$ units are formally a conjugate acid-base pair, the formation of *m*-$Ag_2Mo_2O_7$ theoretically occurs according to equation 1.

$$2\ Ag_2Mo_3O_{10}\cdot 2H_2O + 2\ Ag^+ + 2\ OH^- \rightarrow 3\ Ag_2Mo_2O_7 + 5\ H_2O \quad (1)$$

Both temperature and time have a significant influence on the purity and the morphology of the *m*-$Ag_2Mo_2O_7$ particles. As displayed in Figure 2, when the synthesis is carried out at 35°C for 3h, the powder X-ray diffraction (PXRD) analysis (Figure 2a) reveals that the obtained solid contains a mixture of unreacted

View Article Online
DOI: 10.1039/C8TC02170C

$Ag_2Mo_3O_{10}·2H_2O$ and a second intermediate phase that has been identified as Ag_2MoO_4 (JCPDS card No. 08-0473). In these conditions, its formation from $Ag_2Mo_3O_{10}·2H_2O$ seems to be kinetically favored compared to that of *m*-$Ag_2Mo_2O_7$ and might originate from a second reaction that formally requires an $Ag^+/Ag_2Mo_3O_{10}·2H_2O$ ratio of 4:1 (equation 2). However as this latter was initially fixed to 1:1, almost only one fourth of the initial amount of $Ag_2Mo_3O_{10}·2H_2O$ can be really converted to Ag_2MoO_4, and hence, the mixture finally contains $Ag_2Mo_3O_{10}·2H_2O$ and Ag_2MoO_4 in equal proportions.

$$Ag_2Mo_3O_{10}·2H_2O + 4\ Ag^+ + 4\ OH^- \rightarrow 3\ Ag_2MoO_4 + 4\ H_2O \quad (2)$$

When the previous mixture is heated at 70°C for 1h (Figure 2b), $Ag_2Mo_3O_{10}·2H_2O$ and Ag_2MoO_4 react together to reach *m*-$Ag_2Mo_2O_7$ according to equation 3, and the conversion is complete within 3h (Figure 2c).

$$Ag_2Mo_3O_{10}·2H_2O + Ag_2MoO_4 \rightarrow 2\ Ag_2Mo_2O_7 + 2\ H_2O \quad (3)$$

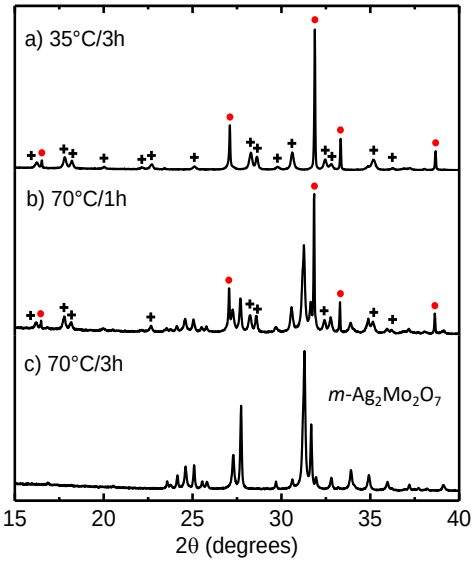

Figure 2. PXRD patterns of silver molybdates obtained under ambient pressure from $Ag_2Mo_3O_{10}·2H_2O$ NWs and one fold of Ag^+ ions in an aqueous basic medium at (a) 35°C/3h, (b) 70°C/1h and (c) 70°C/3h. The non-indexed diffraction peaks correspond to *m*-$Ag_2Mo_2O_7$. Peaks labelled with red circles and black crosses are assigned to Ag_2MoO_4 and $Ag_2Mo_3O_{10}·2H_2O$ impurities, respectively.

The purity and crystallinity of the *m*-$Ag_2Mo_2O_7$ NWs were confirmed by PXRD analysis at room temperature and the Rietveld refinement was performed using the published $P2_1/c$ structural model[38] (Figure S1, ESI†). In good agreement with a nanowire-like shape of the material (see below), an anisotropic crystal size was determined to be ~93.0(3) and ~70.0(5) nm along and perpendicular to the running axis of the crystallites, respectively. The SEM and TEM images (Figures 3a and 3b) show uniform NWs with a mean diameter around 100 nm and lengths up to several tens of micrometres. Noticeably, the use of a nanostructured precursor as well as the weak temperature and pressure conditions strongly limit the crystal growth of the *m*-$Ag_2Mo_2O_7$ NWs that exhibit a specific surface area of 9.8 m^2/g i.e., 5-fold higher than the reported values.[40] Furthermore, we confirmed that hydrothermal treatments strongly damage the nanostructuration of *m*-$Ag_2Mo_2O_7$. Indeed, when the synthesis was carried out under very mild hydrothermal conditions (100°C/3h) (see Supporting Information for the detailed synthesis), the obtained particles exhibit a microrod-like shape (Figure S2, ESI†), and their specific surface area dramatically drops to 2.4 m^2/g. The hydrothermal conditions also impact on the structure of the nanomaterial by favouring the polymorphous conversion from *m*-$Ag_2Mo_2O_7$ to *t*-$Ag_2Mo_2O_7$. Typically, PXRD patterns of solids obtained from different hydrothermal treatments (Figure S3, ESI†) reveal that the formation of *t*-$Ag_2Mo_2O_7$ arises from 100°C/6h, and its amount progressively increases with increasing both temperature and time. In stark contrast, TGA/DSC measurements performed on a dry powder of *m*-$Ag_2Mo_2O_7$ NWs indicate that the polymorphous transformation does not occur in air by only increasing the temperature (Figure S4, ESI†). Indeed, the DSC curve does not show any transition before the material melts congruently at 516°C.[41] From a structural point of view, *m*- and *t*-$Ag_2Mo_2O_7$ are built upon the same polymeric 1D-$[Mo_2O_7]^{2-}$ unit running along the a axis, but the relative orientation of the molybdate chains and the positioning of the silver cations differ (Figure 1b). This strong structural change suggests very high free energy barrier for the conversion of both polymorphs, and could explain why they cannot be thermally transformed in the solid state. However the density of *m*-$Ag_2Mo_2O_7$ (5.796) is slight lower than that of *t*-$Ag_2Mo_2O_7$ (5.873), and hence, at first sight, the polymorphous conversion observed by increasing the temperature of the hydrothermal treatment could actually originate from the increase of the autogenous pressure in the autoclave.

Optical absorption properties of the *m*-$Ag_2Mo_2O_7$ NWs were investigated in ambient conditions by UV-vis diffuse reflectance spectroscopy (Figure S5, ESI†). This material exhibits an optical band gap of 3.0 eV (413 nm) that is slightly blue-shifted compared to other reported values (2.7-2.9 eV).[26–28] This is well consistent with the reduced thickness of the NWs, and it reveals the presence of quantum confinement of the photogenerated electron-hole carriers into the 1D-nanomaterial.[42] As already described,[27,28] the valence band is mainly composed of the hybridization of Ag 4d and O 2p states while the bottom of the conduction band is mainly formed by the hybridization of Mo 4d and O 2p states (Figure S5, ESI†). The Ag 4d orbitals usually act as a sub-band lying above the O 2p orbitals at the top of the valence band, and hence, the optical band gap results in a strong Ag to Mo charge transfer.

Design and morphology of the Ag@*m*-$Ag_2Mo_2O_7$ nanostructure. Figure 3b and Figure S6, ESI† display TEM images at different scales of the surface morphology of the m-$Ag_2Mo_2O_7$ NWs once irradiated under UV-light (365 nm) for 40 min. Small quasi-spherical NPs with an average diameter of 5 nm randomly decorates the surface of the NWs which have well maintained their initial morphology. To better characterized the nature of the NPs, they were investigated by

View Article Online
DOI: 10.1039/C8TC03170C

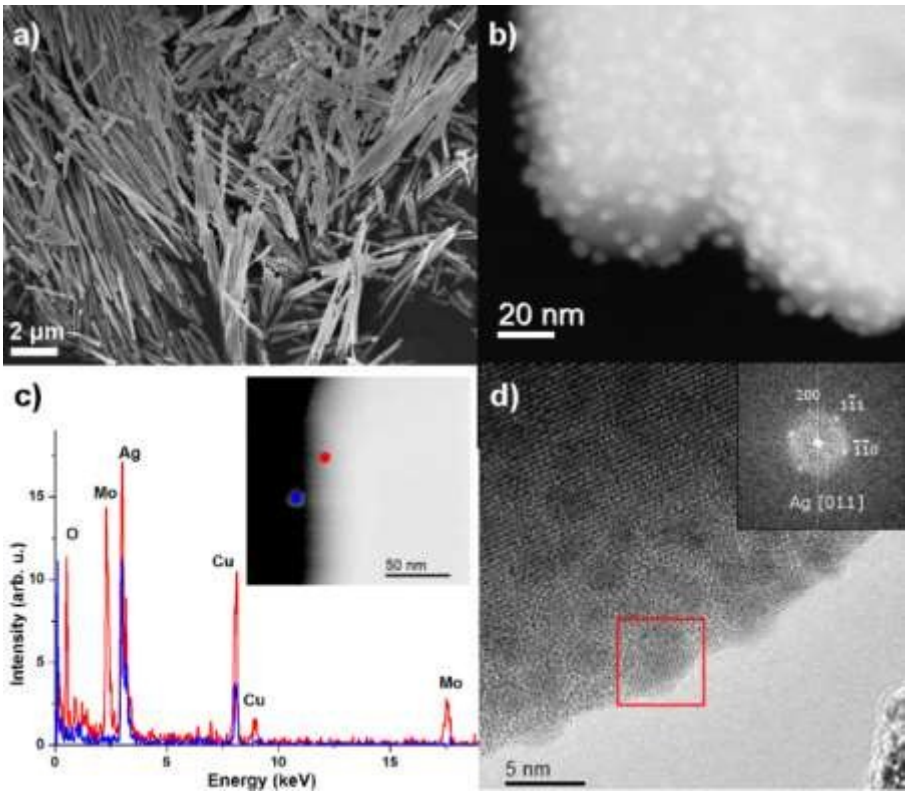

Figure 3. a) SEM image of the very thin *m*-$Ag_2Mo_2O_7$ NWs. b) STEM-HAADF micrograph of *m*-$Ag_2Mo_2O_7$ NWs after UV irradiation (365 nm) for 40 min. c) EDS spectra acquired on the NP (blue) and on the NW (red) corresponding to the area highlighted by the blue and red circles shown in the STEM-HAADF image displayed in the inset. d) Cs corrected HR-TEM image of the surface of a NW after UV irradiation. The red square highlights the area used to determine the FFT depicted in the inset. The successful indexation of the FFT was obtained with the Ag face-centred cubic structural data in the [011] zone axis.

a combination of energy X-ray dispersive spectroscopy (EDS) and HR-TEM techniques, which is a powerful tool to extract structural and chemical information at the nanoscale.[43,44] The EDS spectra were recorded on the NPs and compared to those obtained on the NWs (Figure 3c). While the NWs show the presence of Ag, O and Mo lines (and also Cu coming from the TEM grid), only the Ag line is observed for the NPs. The HR-TEM micrograph and the corresponding FFT pattern (Figure 3d) reveal the high degree of crystallinity of the photogenerated nanoparticles. The successful indexation of the FFT pattern (inset of Figure 3d) obtained from the highlighted area shows that the NP corresponds to the Ag face-centred cubic structure. It is also worth noticing that the irradiation leads to the formation of an amorphous 3-4 nm-thick layer (Figure S7, ESI†), indicating that the surface of the NWs is slightly modified after the photogeneration of the Ag NPs. It is worth noticing that the Ag@*m*-$Ag_2Mo_2O_7$ nanostructure is relatively stable over time with no observed degradation during the storage.

Figure 4a shows the XPS Ag 3d spectra of the *m*-$Ag_2Mo_2O_7$ NWs before and after irradiation under UV light (365 nm, 40 min). To extract more quantitative information, a modelling of the spectra is presented in Figure S8, ESI†. The binding energy of the Ag $3d_{5/2}$ is at 368.1 eV and the splitting between the $3d_{5/2}$ and $3d_{3/2}$ lines is equal to 6.0 eV. After irradiation another contribution of similar intensity can be clearly seen for which the Ag 3d lines are shifted to higher energy by 0.7 eV. This shift can be ascribed to the presence of Ag metallic states.[45] Examination of Auger spectra is also useful to identify Ag chemical states.[23,24,46] The irradiation leads to the modification of the fine structures of the $M_{4,5}N_{4,5}N_{4,5}$ Auger electron spectrum (Figure S9, ESI†) which exhibits two additional peaks at 357.3 eV and 351.3 eV assignable to metallic silver.[46] Moreover, the modified Auger α parameters (summation of the kinetic energy of the Auger transition and the binding energy of the core level) of the *m*-$Ag_2Mo_2O_7$ NWs and of the new contribution after irradiation are equal to 723.6 and 726.1, respectively. This last value well corresponds to the Ag^0 valence state.[46] It should be noted that the Mo 3d shape and binding energy remain unchanged after UV irradiation (Figure S10, ESI†). Finally, the XPS valence band spectra are shown in Figure 4b. Before UV irradiation, the valence band is made up of a unique broad band in the 2–10 eV energy with a maximum located at around 5 eV. The maximum position nicely corresponds to Ag 4d states.[47] After UV irradiation, the valence band increases in intensity and metallic states are observed near the Fermi level. These latter are closed to those reported for silver metal.[48] All these

findings confirmed that Ag^+ cations are photo-reduced and the resulting Ag^0 atoms aggregate at the surface of the NWs.

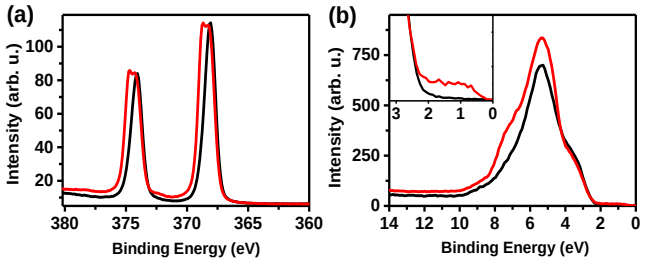

Figure 4. a) XPS Ag 3d spectra of the m-$Ag_2Mo_2O_7$ NWs before (black line) and after (red line) UV irradiation (365 nm, 40 min). b) Valence band XPS spectra of the m-$Ag_2Mo_2O_7$ NWs before (black line) and after (red line) irradiation. The inset shows a magnified view of the same spectra between 0 and 3 eV.

All these results highlight that the Ag@*m*-$Ag_2Mo_2O_7$ nanostructure is easily obtained by exposing the photosensitive *m*-$Ag_2Mo_2O_7$ NWs under low-power UV irradiation (365 nm, 6 W). As expected, the 1D-$[Mo_2O_7]^{2-}$ unit is more easily photoreducible than the 1D-$[Mo_3O_{10}]^{2-}$ one, and in comparison, higher energy UV-light (254 nm, 6 W) and longer irradiation time (4h) are required to generated Ag NPs at the surface of the $Ag_2Mo_3O_{10}{\cdot}2H_2O$ NWs.[24] The formation of the Ag@*m*-$Ag_2Mo_2O_7$ hybrid nanostructure might occur according to a mechanism based on that proposed for Ag@$Ag_2Mo_3O_{10}{\cdot}2H_2O$.[24] Considering the electronic structure of *m*-$Ag_2Mo_2O_7$ described above, the photo-induced charge carriers lead to the concomitant formation of Mo^{5+} cations and high-oxidizing Ag^{2+} intermediary species. The presence of Mo^{5+} ions was not clearly evidenced by XPS but this could be explained considering the large quantity of Ag photodeposited at the surface of the NWs which makes it more difficult to detect photo-reduced molybdenum centres. In the case of $Ag_2Mo_3O_{10}{\cdot}2H_2O$, Ag^{2+} ions oxidize the neighbouring crystallized water molecules to O_2 and protons, and generate Ag^0 atoms which aggregate into Ag NPs. The protons are then transferred onto the adjacent 1D-$[Mo_3O_{10}]^{2-}$ units to create hydroxyl groups which stabilize the photoreduced Mo^{5+} cations. *m*-$Ag_2Mo_2O_7$ does not contain any crystallized water molecules but the high specific surface area of the NWs must favour adsorption of water molecules which can be easily photoreduced at the surface of molybdenum oxides.[49] Comparison of the near-infrared spectra of *m*-$Ag_2Mo_2O_7$ before and after UV irradiation reveals the loss of adsorbed water molecules in the Ag@*m*-$Ag_2Mo_2O_7$ nanostructure (Figure S11, ESI†). Consequently, we may assume that the photo-reduction of Ag^{2+} and Mo^{6+} ions in the *m*-$Ag_2Mo_2O_7$ NWs might be coupled with the oxidation of adsorbed water molecules.

Plasmonic activity of the Ag@*m*-$Ag_2Mo_2O_7$ nanostructure. Figure 5 displays the evolution of the absorption spectrum of the *m*-$Ag_2Mo_2O_7$ NWs upon UV irradiation at 365 nm. The color of the powdered sample gradually shifts from pale yellowish-white to grey with increasing irradiation time. The color change deals with the appearance of a broad absorption band at λ = 462 nm with a shoulder peaking around λ = 795 nm. These absorptions grow up and reach a saturation level after about 40 min (Figure S12, ESI†). Similarly as observed for Ag@$Ag_2Mo_3O_{10}{\cdot}2H_2O$,[24] these bands can be ascribed to both the LSPR of silver NPs and the photogenerated Mo^{5+} cations into the 1D-$[Mo_2O_7]^{2-}$ chains. Their amounts at the surface of the NWs gradually increase under UV-light and reach their maximum after 40 min.

View Article Online DOI: 10.1039/C8TC03170C

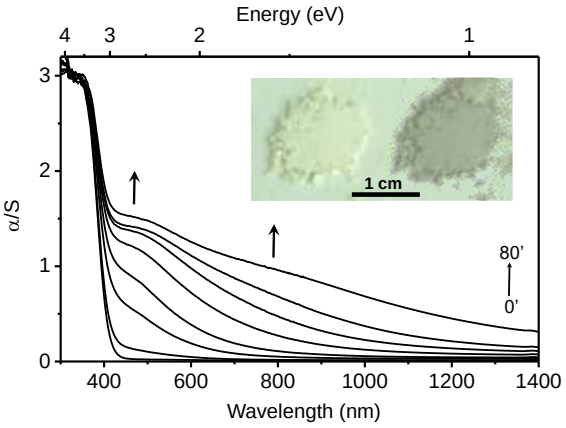

Figure 5. Evolution of the photogenerated absorption of the *m*-$Ag_2Mo_2O_7$ NWs after 0, 1, 5, 10, 20, 30, 40, and 80 min of UV irradiation (365 nm – 6W). Insert: photographs of the *m*-$Ag_2Mo_2O_7$ NWs before (left) and after (right) UV-light irradiation (365 nm) for 1 h.

Figure 6a shows the STEM-HAADF micrograph of a nanowire after UV irradiation. This objet has a complex geometry: the surface of the nanowire is decorated with small Ag nanoparticles of different size (2-6 nm, and below). The nanoparticles are randomly, disorderly-driven, 3D-organized at the surface of the NW. (S)TEM-EELS is a powerful technique for investigating the plasmonic response of nanostructures,[50–53] and then we have carried out such kind of experiments on these nano-objects. The red squares in Figure 6a and Figure 6b highlight the area used for the SR-EELS analysis. Figure 6c shows the EELS response at the vicinity of the Ag@*m*-$Ag_2Mo_2O_7$ nanostructure. The EELS response is mainly dominated by one peak (labelled B in Figure 6c) at 3.35 eV (370 nm). The energy position of the B feature is in good agreement with the LSPR of quantum-size silver nanoparticles.[51,54] At lower energy, between 1.1 and 3.0 eV, another feature (labelled A in Figure 6c) can be highlighted. The A feature can also clearly be seen on the spectra before ZLP deconvolution (Figure S13, ESI†). Contrary to the B feature, the A feature is continuous and shapeless. It should correspond to a sum of continuous energy-loss processes. The physical origin of these processes is not certain at the moment but it can include various effects such as quantum tunnelling between close NPs and effects related to coalescence,[55] additional plasmon resonances already observed for ultra small silver NPs,[56] different contributions related to the response of NPs' size distribution and the influence of the nanowire substrate on the silver LSPR.[51,57] It should be noted that the signature of the bulk plasmon peak (at 3.85 eV) cannot be highlighted in the dataset. This is in good agreement with what has been already observed for silver nanoparticles smaller than 6 nm.[54] Figures 6d and 6e show the map of the integrated intensity of the features B and A, respectively. The exaltation of the silver LSPR at the tip of the NW can clearly be highlighted from Figure 6d. The silver surface plasmon is mainly localized in the first 10 nanometres of vacuum above the NW surface. Interestingly, despite the random coverage of the silver

View Article Online
DOI: 10.1039/C8TC03170C

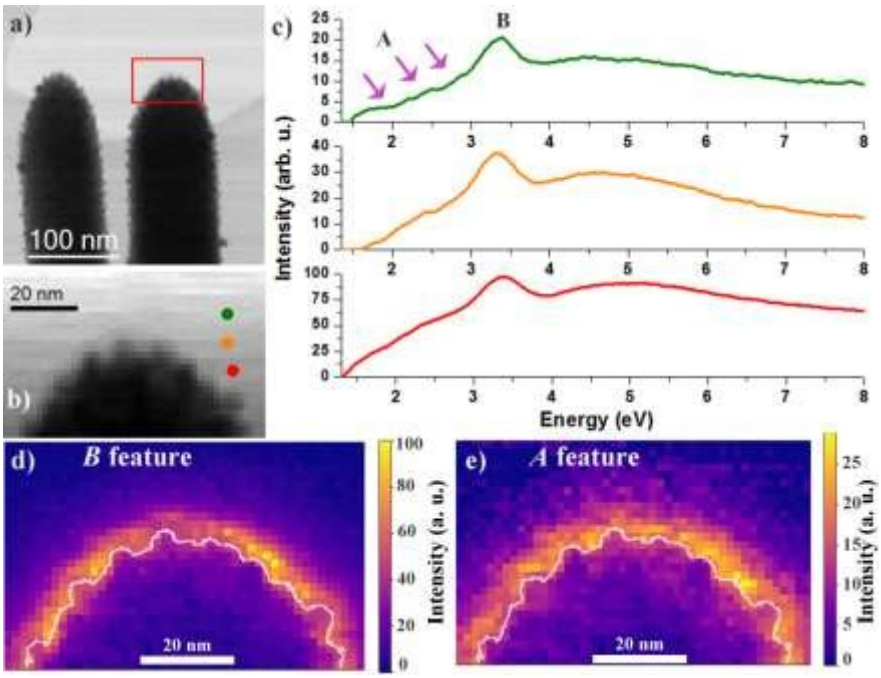

Figure 6. a) STEM-ABF micrograph of the Ag@*m*-$Ag_2Mo_2O_7$ hybrid nanostructure. The red square highlights the area used for the SR-EELS analysis. b) STEM-ABF image acquired at the same time than the SR-EELS analysis. The green, orange and red dots correspond to the areas in which the green, orange and red EELS spectra of c) have been monitored. c) Low-loss EELS spectra acquired with the monochromator excited and extracted from the SR-EELS dataset. The violet arrows highlight the presence of the A feature at low energy. d-e) Map of the integrated intensity of the B and A features, respectively. The white lines highlight the surface contour of the Ag@*m*-$Ag_2Mo_2O_7$ nanostructure.

NPs at the surface of the NW, the LSPR cover the whole surface of the NW. Some hot-pots of higher intensity localized over few nanometres are also present at the surface of the NW. This is similar to what has already been observed on disordered semi-continuous silver films.[58] The spectral weight of the A feature is roughly equal to 1/3 of the spectral weight of the B feature. It is also localized mainly at the surface of the heterostructure which confirms its surface nature. From these observations it can be concluded that, after UV irradiation, the plasmonic Ag@*m*-$Ag_2Mo_2O_7$ nanostructure acts as a single resonator for a broad range of wavelengths with intense, extremely localized and widely distributed electric fields. Then the electric field localization was probed by another optical method i.e., the Raman spectroscopy. Indeed the nanostructuration of the Ag@*m*-$Ag_2Mo_2O_7$ nanostructure should constitute a natural source of field enhancement for surface enhanced Raman scattering (SERS) if silver NPs are accessible to small molecules. Therefore a SERS study of this new plasmonic substrate was investigated by using the SERS molecular probe, 2,2'-bipyridine.[59] Several wavelengths (488.00, 514.53, 632.80 and 785.00 nm) of Raman excitation were used but only the results obtained with a green excitation (514.53 nm i.e. 2.41 eV) are discussed here because the SERS effect was the strongest at this wavelength. At 488.00 nm, samples were damaged and at 632.80 or 785.00 nm, no enhancement and no change of the background were displayed. Moreover this green excitation corresponds to the A feature (around 2.4 eV) positioned at the edge of the principal plasmonic resonance in the EELS spectra (Figure 6). Figure 7 displays the Raman spectra of the *m*-$Ag_2Mo_2O_7$ NWs coated onto a pure silica glass, before and after 365-nm UV irradiation for 1h. Before UV exposure, the Raman spectrum of the NWs in the 600-1800 cm^{-1} range exhibits an intense line at 906 cm^{-1} and other weak lines at 881, 854, 829, 817, 761, and 696 cm^{-1}. Upon UV irradiation, the Raman spectrum of the Ag@*m*-$Ag_2Mo_2O_7$ nanostructure displays the increase of a large "background" signal centred on 1200 wavenumbers Raman shift, i.e. in absolute, around 2.26 eV, which quite confirms the apparition of resonant plasmonic structures. The SERS effect was highlighted (Figure 8) using an aqueous solution containing 0.7 µM 2,2'-bipyridine, with focused laser incident irradiances lower than 5 µW/µm^2. The SERS spectrum is representative of all of the spectra collected at different area. In the range 1100-1800 cm^{-1}, the obtained profile shows four main bands around 1595, 1570, 1490 and 1320 cm^{-1} and is similar to the usual SERS signature of physisorbed 2,2'-bipyridine molecules[60,61,62] obtained with nano-silver colloids deposited directly from an aqueous suspension (blue spectrum in Figure 8). The Ag_x-N bonds were displayed (not shown here) at around 230-250 cm^{-1}, confirming the direct interaction between molecular probes and surface silver atoms of the nanoparticles. Even if 2,2'-bipyridine is not the best molecular probe to reach very strong enhancement, this study well evidences the presence of aggregates of metallic silver NPs in

View Article Online
DOI: 10.1039/C8TC03170C

the Ag@*m*-$Ag_2Mo_2O_7$ plasmonic hybrid nanocomposite. In addition, the observation of a SERS effect confirms the integrity of the nanostructure when immersed in the molecular probe aqueous solution.

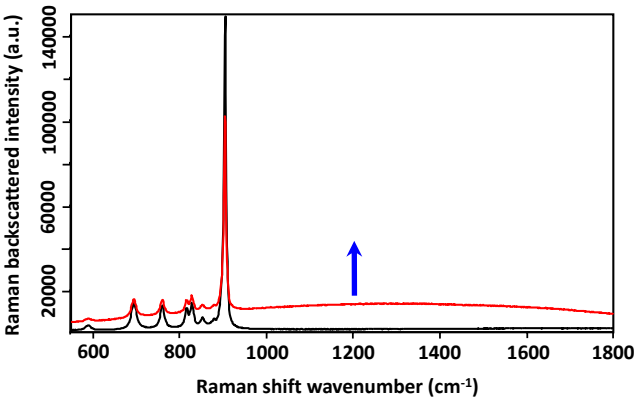

Figure 7. Raman spectra of the *m*-$Ag_2Mo_2O_7$ NWs before (black line) and after (red line) UV-light irradiation (365 nm) for 1h. The "background" signal between 1000 and 1800 cm^{-1} increased under UV irradiation. The energy corresponding of this signal is centered at 2.26 eV (blue arrow).

Now in order to control and to quantify the SERS effect, further efforts will be devoted to the synthesis of controlled thin film substrates based on this material, and also to in-depth SERS studies with different molecular probes at different excitation wavelengths in order to investigate the SERS mechanisms (enhancement by only localised electric field like in a shiners composite or chemical effect by creating new electronic level or by charge transfer, etc..) as recently applied with metal oxides.[63,64,65]

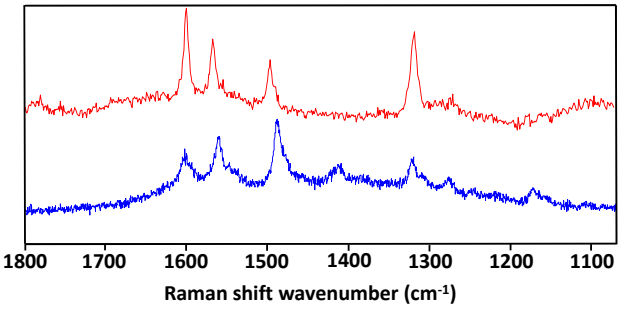

Figure 8. SERS spectrum of 2-2'-bipyridine adsorbed on the Ag@*m*-$Ag_2Mo_2O_7$ substrate (red line) compared with a usual SERS spectrum (blue line) obtained on a colloidal aggregates deposited on a silica glass.

Conclusions

To conclude, we have succeeded in designing pure very thin photosensitive *m*-$Ag_2Mo_2O_7$ NWs via a new soft-chemistry route under ambient pressure. Through the use of both a nanostructured precursor and weak temperature and pressure conditions, the obtained *m*-$Ag_2Mo_2O_7$ NWs exhibit a specific surface area higher than those reported from other reported synthesis methods. Hydrothermal treatments, even at low temperature, dramatically damage the morphology of the *m*-$Ag_2Mo_2O_7$ NWs, and they also favour their pressure-driven monoclinic to triclinic polymorphous conversion. The Ag@*m*-$Ag_2Mo_2O_7$ plasmonic hybrid nanostructure was then easily *in situ* obtained via a solid-state photodeposition method, by exposing the photosensitive *m*-$Ag_2Mo_2O_7$ NWs under low-power UV-light. Strikingly, compared with our previously reported Ag@$Ag_2Mo_3O_{10}{\cdot}2H_2O$ nanocomposite, the deposition of Ag NPs at the surface of the *m*-$Ag_2Mo_2O_7$ NWs requires a lower UV-energy and shorter irradiation duration. The plasmonic activity of the Ag@*m*-$Ag_2Mo_2O_7$ hybrid nanostructure has been well evidenced by a combination of UV-vis, SR-EELS and Raman spectroscopies revealing that the nanocomposite acts as a single resonator for a broad range of wavelengths. It was also demonstrated as an efficient SERS-active nanocomposite by using the molecular probe 2,2'-bipyridine.

Experimental section

Synthesis. All chemicals and reagents were purchased from major chemical suppliers and used as received except $Ag_2Mo_3O_{10}{\cdot}2H_2O$ NWs which has been synthesized according to the reported procedure.[24]

***m*-$Ag_2Mo_2O_7$ NWs.** $Ag_2Mo_3O_{10}{\cdot}2H_2O$ (300 mg, 0.429 mmol) was introduced in 25 mL of water. After addition of $AgNO_3$ (73 mg, 0.429 mmol), the mixture was stirred at room temperature, and 4.30 mL of NaOH 0.1 M was added dropwise. The mixture was heated at 70°C and stirred for 3 h. After filtration, the resulting yellowish-white solid (the final pH of the solution was 6.3) was washed with H_2O, EtOH, and dried in air. Yield in Mo: 95%. FT-IR (cm^{-1}): ν(Mo=O, Mo-O-Mo), 930 (w), 907 (s), 889 (s), 880 (s), 839 (s), 754 (s), 704 (s), 642 (m), 563 (v), 486 (m), 457 (sh), 408 (w).

Ag@*m*-$Ag_2Mo_2O_7$. The plasmonic hybrid nanostructure was obtained by irradiating the *m*-$Ag_2Mo_2O_7$ NWs with a Fisher Bioblock labosi UV lamp (λ_{exc} = 365 nm, 6 W) for 40 min.

Physical Measurements. Pure powder material was examined by X-ray diffraction using a D8 Bruker diffractometer in the Bragg-Brentano geometry, equipped with a front germanium monochromator, a copper anode (Cu*K*-L3 radiation, λ=1.54059 Å) and a LynxEye PSD detector. Nitrogen volumetric measurement treated by the Brunauer-Emmett-Teller (BET) approaches were recorded on a micrometrics ASAP 2010 device. FT-IR spectra in the MIR range were recorded on a BRUKER Vertex equipped with a computer control using the OPUS software. Differential scanning calorimetry (DSC) and thermogravimetric analysis (TGA) were performed by flowing dry argon on a SETARAM TG-DSC 111. Raman spectra were recorded using a microconfocal Raman Invia Reflex device. The instrument was equipped with a double edge filter to eliminate the Rayleigh scattering, and a Charged Couple Device (CCD) camera working at a temperature of 220 K with a 1024 by 256 pixels array. Laser excitations were at 488.00, 514.53 nm, 632.80 nm and 785.00 nm. The irradiation at 488.00 nm was too near the edge of the optical absorption of the silver molybdate NWs and strongly damaged the samples. Consequently, only three wavelengths were used to probe the SERS of 2,2'-bipyridine and to find the maximum SERS effects without other resonance effect. The spectral resolution achieved with the use of gratings of 2400, 1800

or 1200 grooves per millimeter was between 3 and 4 cm^{-1} according to the excitation wavelength. The focused power of the laser beam was also checked for each wavelength to avoid any transformation or heating of the samples. SERS effects were observed to be strongest with a laser excitation at 514.53 nm. The incident laser beam was focused to keep an irradiance lower than 5 $\mu W/\mu m^2$. If the laser power is increased, some damages were observed, underlined in the Raman spectra, by the apparition of amorphous carbon spectra. Accordingly, the power was kept below 100 µW and the magnitude × 20 of the objective has been selected after a test list. The spatial probed area by × 20 objective was then around 10 μm^2 in order to average our results recorded on the deposited powders. The confocal mode with x100 objective was also sometimes used to select a smaller analyzed volume in the same irradiated volume or to record Raman maps with the better spatial resolution (around at $\lambda/2$). SERS substrates were obtained by coating pure silica glasses with drops of *m*-$Ag_2Mo_2O_7$ NWs dispersed in ethanol. The coated slides were dried under ambient conditions. Drops of aqueous solution containing 0.7 µM 2,2'-bipyridine were then deposited onto the substrates. Samples studied in this paper were heterogeneous at the micrometer scale. For comparison of our Raman results, we have used colloidal dispersion of nanoparticles of silver synthesized by the usual method in aqueous medium by reduction of an $AgNO_3$ containing solution by $NaBH_4$. The Ag^0 NPs characterized by a diameter around 15 nm ± 7 nm was either deposited on a pure silica glass or used directly in suspension in contact with 2,2'-bipyridine molecules. Diffuse reflectivity spectra in the UV-Visible range were collected with a Cary 5G spectrometer (Varian) equipped with a 60 mm diameter integrating sphere and computer control using the "Scan" software. The X-ray photoelectron spectroscopy (XPS) analyses were carried out using Kratos Axis Supra spectrometer. The photoelectron spectra were excited by a soft X-ray Al Kα (1486.6 eV) anode at a power of 225 W (15 mA, 15 kV). Short measurements were performed before and after the measurements presented here to be sure that the sample was not modified by the X-ray radiation. Calibration of the spectra was done by setting the position of the C1s peak coming from carbon-based contaminants at 284.9 eV. Scanning electron microscopy (SEM) images were taken in a high-magnification microscope JEOL JSM-6400F. For SEM studies, samples were prepared by spreading a small amount of powder on a carbon tape pasted over a copper metal sample holder. Preliminary transmission electron microscopy (TEM) experiments were performed on a Hitachi HF 2000 (Field Emission Gun, 100 KV) with a probe diameter of about 7 nm. Irradiation was performed ex-situ by directly positioning the TEM sample holder under a UV-lamp (365 nm, 6W) for 40 min, to ensure the complete irradiation of all the probed material. Moreover, samples before and after UV irradiation were cooled down at liquid nitrogen temperature to prevent the growth of Ag^0 nanoparticles under electron beam irradiation and carbon contamination. Aberration corrected high-resolution scanning transmission electron microscopy (HR-STEM) experiments have been performed using a FEI Titan Low-Base microscope operated at 80 kV and equipped with a CESCOR Cs probe corrector, an ultra-bright X-FEG electron source, a monochromator and an energy-dispersive X-ray spectroscopy (EDS) detector. HR-STEM imaging was performed by using high-angle annular dark field (HAADF) and annular bright field (ABF) detectors. Spatially-resolved EELS (SR-EELS) experiments were performed with the monochromator excited to check the plasmonic properties of the heterostructure. The energy resolution was 240 meV with a dispersion of 0.02 eV per pixel and the acquisition time was about 0.35 sec per pixel (total acquisition time ~ 8 min). The acquisition parameters were carefully chosen to maximize the signal on noise ratio while ensuring a short acquisition time in order to prevent strong spatial drift which are a common occurrence while doing TEM measurements at liquid N_2 temperature. The dataset was then aligned on the energy scale by using the zero-loss peaks (ZLP) as reference. The dataset was denoised by using the principal component analysis routines of the hyperspy software.[66] The Richardson-Lucy deconvolution algorithm was employed to improve the energy resolution.[67,68] For this purpose the point spread function was determined by using 45 aligned ZLP spectra recorded far away from the nanowire. The number of iterations was limited to 3 to avoid the introduction of artefacts. After this process the energy resolution was improved to 180 meV. The ZLP was subtracted from the dataset by using the 45 aligned ZLP taken in the vacuum after deconvolution. This procedure is shown in the Figure S13a, ESI†, and was already successfully used to determine the band-gap of Mo-based nanostructures.[69] The B feature at 3.35 eV (see text below for more details) was fitted by using a Gaussian function as shown in the Figure S13b, ESI†. The map corresponding to the integrated intensity of the B feature was created by area integration of the Gaussian function along the whole dataset. After subtraction of the Gaussian function from the dataset, the map of the A feature at lower energy was determined by area integration between 1.1 and 3.35 eV (Figure S13b, ESI†). Finally the two maps were normalized by using the maximum value of the map corresponding to the B feature. Additional HR-TEM measurements were performed by using a FEI Titan Cube microscope operating at 80 kV and equipped with a Cs image corrector. Interpretations of the Fourier transform (FFT) patterns obtained on were performed using the JEMS software. All the (S)TEM experiments were performed at liquid nitrogen temperature to prevent the growth of Ag^0 nanoparticles under electron beam irradiation and to hinder carbon contamination and electron beam damages.

Acknowledgements

The authors thank Houda El Bekacchi for the achievement of the first exploratory syntheses. This work was supported by CNRS and by Ministère de l'Education Nationale, de l'Enseignement Supérieur et de la Recherche. The STEM, HR-(S)TEM, EDS and SR-EELS studies were conducted at the Laboratorio de Microscopias Avanzadas, Instituto de Nanociencia de Aragon, Universidad de Zaragoza, Spain. L. Lajaunie acknowledges Dr. Guillermo Antorrena (INA, Zaragoza) for the XPS measurements and fruitful discussions.

Funding sources

R.A. gratefully acknowledges the support from the Spanish Ministerio de Economia y Competitividad (MAT2016-79776-P),

from the Government of Aragon and the European Social Fund under the project "Construyendo Europa desde Aragon" 2014-2020 (grant number E/26) and from the European Union H2020 program ETN project "Enabling Excellence" Grant Agreement 642742.

References

1 Y.-C. Pu, G. Wang, K.-D. Chang, Y. Ling, Y.-K. Lin, B. C. Fitzmorris, C.-M. Liu, X. Lu, Y. Tong, J. Z. Zhang, Y.-J. Hsu and Y. Li, *Nano Lett.*, 2013, **13**, 3817–3823.

2 Y.-C. Yen, P.-H. Chen, J.-Z. Chen, J.-A. Chen and K.-J. Lin, *ACS Appl. Mater. Interfaces*, 2015, **7**, 1892–1898.

3 T. D. Dao, G. Han, N. Arai, T. Nabatame, Y. Wada, C. V. Hoang, M. Aono and T. Nagao, *Phys. Chem. Chem. Phys.*, 2015, **17**, 7395–7403.

4 A. Kolmakov and M. Moskovits, *Annu. Rev. Mater. Res.*, 2004, **34**, 151–180.

5 G. Shen, P.-C. Chen, K. Ryu and C. Zhou, *J. Mater. Chem.*, 2009, **19**, 828–839.

6 W. Ye, R. Long, H. Huang and Y. Xiong, *J. Mater. Chem. C*, 2017, **5**, 1008–1021.

7 M. Feng, M. Zhang, J.-M. Song, X.-G. Li and S.-H. Yu, *ACS Nano*, 2011, **5**, 6726–6735.

8 H. Tang, A. Lu, L. Li, W. Zhou, Z. Xie and L. Zhang, *Chem. Eng. J.*, 2013, **234**, 124–131.

9 I. S. Grover, R. C. Prajapat, S. Singh and B. Pal, *Sol. Energy*, 2017, **144**, 612–618.

10 M. C. Ortega-Liebana, J. L. Hueso, R. Arenal and J. Santamaria, *Nanoscale*, 2017, **9**, 1787–1792.

11 X. Zhao, P. Wang, Z. Yan and N. Ren, *Chem. Phys. Lett.*, 2014, **609**, 59–64.

12 T. Kawawaki, H. Wang, T. Kubo, K. Saito, J. Nakazaki, H. Segawa and T. Tatsuma, *ACS Nano*, 2015, **9**, 4165–4172.

13 M.-Y. Lu, C.-Y. Tsai, H.-A. Chen, Y.-T. Liang, K.-P. Chen, S. Gradečak, S. Gwo and L.-J. Chen, *Nano Energy*, 2016, **20**, 264–271.

14 T. Kang, S. M. Yoo, I. Yoon, S. Y. Lee and B. Kim, *Nano Lett.*, 2010, **10**, 1189–1193.

15 X.-J. Chen, G. Cabello, D.-Y. Wu and Z.-Q. Tian, *J. Photochem. Photobiol. C Photochem. Rev.*, 2014, **21**, 54–80.

16 Z. Y. Bao, D. Y. Lei, J. Dai and Y. Wu, *Appl. Surf. Sci.*, 2013, **287**, 404–410.

17 S. M. Prokes, O. J. Glembocki, R. W. Rendell and M. G. Ancona, *Appl. Phys. Lett.*, 2007, **90**, 093105.

18 J. Li, J. Xu, W.-L. Dai and K. Fan, *J. Phys. Chem. C*, 2009, **113**, 8343–8349.

19 P. Wang, B. Huang, Y. Dai and M.-H. Whangbo, *Phys. Chem. Chem. Phys.*, 2012, **14**, 9813.

20 J. Kwon, H. Cho, H. Lee, J. Yeo, S. Hong, S. Han and S. H. Ko, *ECS J. Solid State Sci. Technol.*, 2018, **7**, Q131-Q135.

21 J. Kwon, J. Yeo, S. Hong, Y. D. Suh, H. Lee, J.-H. Choi, S. S. Lee and S. H. Ko, *Energy Technol.*, 2016, **4**, 271-277.

22 J. Kwon, H. Cho, H. Lee, S. Hong, Y. D. Suh, H. Moon, D. Kim, J.-H. Choi, M.-T. Lee, J. Yeo, and S. H. Ko, *ECS J. Solid State Sci. Technol.*, 2015, **4**, P424-P428.

23 M. Karmaoui, L. Lajaunie, D. M. Tobaldi, G. Leonardi, C. Benbayer, R. Arenal, J. A. Labrincha and G. Neri, *Appl. Catal. B Environ.*, 2017, **218**, 370–384.

24 K. Hakouk, P. Deniard, L. Lajaunie, C. Guillot-Deudon, S. Harel, Z. Wang, B. Huang, H.-J. Koo, M.-H. Whangbo, S. Jobic and R. Dessapt, *Inorg. Chem.*, 2013, **52**, 6440–6449.

25 V. Coué, R. Dessapt, M. Bujoli-Doeuff, M. Evain and S. Jobic, *Inorg. Chem.*, 2007, **46**, 2824–2835.

26 J. Wang, P. Guo, M. Dou, J. Wang, Y. Cheng, P. G. Jönsson, Z. Zhao, J. Cao, W. Luo and Z. Li, *RSC Adv.*, 2014, **4**, 51008–51015.

27 D. W. Kim, I.-S. Cho, S. Lee, S.-T. Bae, S. S. Shin, G. S. Han, H. S. Jung and K. S. Hong, *J. Am. Ceram. Soc.*, 2010, **93**, 3867–3872.

28 M. Hashim, C. Hu, C. Zhang and X. Xie, *Phys. E Low-dimensional Syst. Nanostructures*, 2012, **46**, 213–217.

29 M. Hashim, C. Hu, Y. Chen, C. Zhang, Y. Xi and J. Xu, *Phys. status solidi*, 2011, **208**, 1937–1941.

30 M. Hashim, C. Hu, X. Wang, B. Wan and J. Xu, *Mater. Res. Bull.*, 2012, **47**, 3383–3389.

31 D. P. Singh, B. Sirota, S. Talpatra, P. Kohli, C. Rebholz and S. M. Aouadi, *J. Nanoparticle Res.*, 2012, **14**, 781.

32 J. Lin, Q. Wang, Y. Zheng and Y. Zhang, *CrystEngComm*, 2013, **15**, 5668.

33 C.-C. Shen, Q. Zhu, Z.-W. Zhao, T. Wen, X. Wang and A.-W. Xu, *Energy Environ. Sci.*, 2011, **4**, 2922–2929.

34 X. Cui, S.-H. Yu, L. Li, L. Biao, H. Li, M. Mo and X.-M. Liu, *Chem. - A Eur. J.*, 2004, **10**, 218–223.

35 T. Aditya, J. Jana, R. Sahoo, A. Roy, A. Pal and T. Pal, *Cryst. Growth Des.*, 2017, **17**, 295–307.

36 G. Nagaraju, G. T. Chandrappa and J. Livage, *Bull. Mater. Sci.*, 2008, **31**, 367–371.

37 E. K. Fodjo, D.-W. Li, N. P. Marius, T. Albert, Y.-T. Long, C. Zhu, P. K.-H. Tam, J.-F. Chiu and C.-M. Che, *J. Mater. Chem. A*, 2013, **1**, 2558.

38 H.-X. Guo and S.-X. Liu, *Chinese J. Struct. Chem.*, 2005, **24**, 1452–1456.

39 B. M. Gatehouse and P. Leverett, *J. Chem. Soc. Dalt. Trans.*, 1976, **0**, 1316.

40 K. Saito, S. Kazama, K. Matsubara, T. Yui and M. Yagi, *Inorg. Chem.*, 2013, **52**, 8297–8299.

41 E. Wenda, *J. Therm. Anal.*, 1990, **36**, 1417–1427.

42 L. E. Brus, *J. Chem. Phys.*, 1984, **80**, 4403–4409.

43 M. Karmaoui, J. S. Amaral, L. Lajaunie, H. Puliyalil, D. M. Tobaldi, R. C. Pullar, J. A. Labrincha, R. Arenal and U. Cvelbar, *J. Phys. Chem. Lett.*, 2016, **7**, 4039–4046.

44 M. Karmaoui, E. V. Ramana, D. M. Tobaldi, L. Lajaunie, M. P. Graça, R. Arenal, M. P. Seabra, J. A. Labrincha, R. C. Pullar, J. Schubert, D. J. Webb, C. Dieker and J. W. Seo, *RSC Adv.*, 2016, **6**, 51493–51502.

45 S. W. Gaarenstroom and N. Winograd, *J. Chem. Phys.*, 1977, **67**, 3500–3506.

46 V. K. Kaushik, *J. Electron Spectros. Relat. Phenomena*, 1991, **56**, 273–277.

47 L. H. Tjeng, M. B. J. Meinders, J. Van Elp, J. Ghijsen, G. A. Sawatzky and R. L. Johnson, *Phys. Rev. B Condens. Matter Mater. Phys.*, 1990, **41**, 3190–3199.

48 M. P. Seah and I. S. Gilmore, *Surf. Interface Anal.*, 1998, **26**, 908–929.

49 W. B. Faughnan, *RCA Rev.*, 1975, **36**, 177–197.

View Article Online
DOI: 10.1039/C8TC03170C

50 M. Kociak and O. Stéphan, *Chem. Soc. Rev.*, 2014, **43**, 3865.
51 R. Arenal, L. Henrard, L. Roiban, O. Ersen, J. Burgin and M. Treguer-Delapierre, *J. Phys. Chem. C*, 2014, **118**, 25643–25650.
52 B. S. Guiton, V. Iberi, S. Li, D. N. Leonard, C. M. Parish, P. G. Kotula, M. Varela, G. C. Schatz, S. J. Pennycook and J. P. Camden, *Nano Lett.*, 2011, **11**, 3482–8.
53 J. Nelayah, M. Kociak, O. Stephan, F. J. Garcia de Abajo, M. Tence, L. Henrard, D. Taverna, I. Pastoriza-Santos, L. M. Liz-Marzan and C. Colliex, *Nat. Phys.*, 2007, **3**, 348–353.
54 J. A. Scholl, A. L. Koh and J. A. Dionne, *Nat. (London, United Kingdom)*, 2012, **483**, 421–427.
55 J. A. Scholl, A. García-Etxarri, A. L. Koh and J. A. Dionne, *Nano Lett.*, 2013, **13**, 564–569.
56 S. Raza, S. Kadkhodazadeh, T. Christensen, M. Di Vece, M. Wubs, N. A. Mortensen and N. Stenger, *Nat. Commun.*, 2015, **6**, 8788.
57 M. Prieto, R. Arenal, L. Henrard, L. Gomez, V. Sebastian and M. Arruebo, *J. Phys. Chem. C*, 2014, **118**, 28804–28811.
58 A. Losquin, S. Camelio, D. Rossouw, M. Besbes, F. Pailloux, D. Babonneau, G. A. Botton, J.-J. Greffet, O. Stéphan and M. Kociak, *Phys. Rev. B*, 2013, **88**, 115427.
59 Y. Sawai, B. Takimoto, H. Nabika, K. Ajito and K. Murakoshi, *J. Am. Ceram. Soc.*, 2007, **129**, 1658–1662.
60 J. F. Ellena, R. N. Dominey and D. S. Cafiso, *J. Phys. Chem.*, 1987, **91**, 131–137.
61 A. De Bonis, G. Compagnini, R.S. Cataliotti and G. Marletta, *J. Raman Spectrosc*. 1999, **30**, 1067–1071.
62 A.G. Brolo, Z. Jiang and D.E. Irish. *J. Electro. Anal. Chem.*, 2003, **547**, 163–172.
63 S. Cong, Y. Yuan, Z. Chen, J. Hou, M. Yang, Y. Su, Y. Zhang, L. Li, Q. Li, F. Geng and Z. Zhao, *Nat. Commun*. 2015, **6**, 8800.
64 J. Lin, Y. Shang, X. Li, J. Yu, X. Wang and L. Guo, *Adv. Mater*. 2017, **29**, 1604797.
65 J. Lin, W. Hao, Y. Shang, X. Wang, D. Qiu, G. Ma, C. Chen, S. Li and L. Guo, *Small*, **14**, 1703274.
66 F. de la Peña, T. Ostasevicius, V. T. Fauske, P. Burdet, P. Jokubauskas, M. Nord, E. Prestat, M. Sarahan, K. E. MacArthur, D. N. Johnstone, J. Taillon, J. Caron, T. Furnival, A. Eljarrat, S. Mazzucco, V. Migunov, T. Aarholt, M. Walls, F. Winkler, B. Martineau, G. Donval, E. R. Hoglund, I. Alxneit, I. Hjorth, L. F. Zagonel, A. Garmannslund, C. Gohlke, I. Iyengar and H.-W. Chang, DOI:10.5281/ZENODO.583693.
67 A. Gloter, A. Douiri, M. Tencé and C. Colliex, *Ultramicroscopy*, 2003, **96**, 385–400.
68 R. Arenal, O. Stéphan, M. Kociak, D. Taverna, A. Loiseau and C. Colliex, *Phys. Rev. Lett.*, 2005, **95**, 127601.
69 E. D. Hanson, L. Lajaunie, S. Hao, B. D. Myers, F. Shi, A. A. Murthy, C. Wolverton, R. Arenal and V. P. Dravid, *Adv. Funct. Mater.*, 2017, **27**, 1605380.

View Article Online
DOI: 10.1039/C8TC03170C

Table of contents

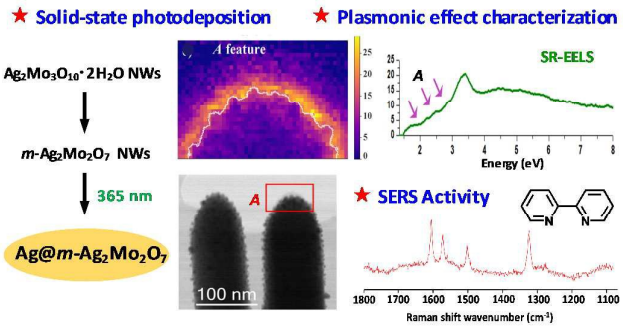

A novel Ag@m-$Ag_2Mo_2O_7$ plasmonic hybrid nanostructure was successfully designed by solid-state photodeposition method from very thin monoclinic *m*-$Ag_2Mo_2O_7$ nanowires obtained via a new soft-chemistry route. The Ag@m-$Ag_2Mo_2O_7$ nanocomposite was demonstrated as an efficient SERS-active material by using the molecular probe 2,2'-bipyridine.